

PAPER • OPEN ACCESS

Linear displacement and force characterisation of a 3D-printed flexure-based delta actuator

To cite this article: Xu Chen *et al* 2022 *Smart Mater. Struct.* **31** 104001

View the [article online](#) for updates and enhancements.

You may also like

- [Cross-shaped piezoelectric beam for torsion sensing](#)
Hojoon Kim, Myotaeg Lim and Youngsu Cha
- [Hybrid piezoelectric-electromagnetic energy harvester for scavenging energy from low-frequency excitations](#)
Kangqi Fan, Qinxue Tan, Haiyan Liu et al.
- [Rotational nonlinear double-beam energy harvesting](#)
Ze-Qi Lu, Fei-Yang Zhang, Hai-Ling Fu et al.

ECS Toyota Young Investigator Fellowship

For young professionals and scholars pursuing research in batteries, fuel cells and hydrogen, and future sustainable technologies.

At least one \$50,000 fellowship is available annually.
More than \$1.4 million awarded since 2015!



Application deadline: January 31, 2023



TOYOTA

Learn more. Apply today!

Linear displacement and force characterisation of a 3D-printed flexure-based delta actuator

Xu Chen^{1,2,*} , Michail E Kiziroglou²  and Eric M Yeatman² 

¹ Hamlyn Center and Department of Electrical and Electronic Engineering, Imperial College London, London SW7 2BX, United Kingdom

² Department of Electrical and Electronic Engineering, Imperial College London, London SW7 2BX, United Kingdom

E-mail: xu.chen18@imperial.ac.uk

Received 24 May 2022, revised 8 August 2022

Accepted for publication 16 August 2022

Published 5 September 2022



Abstract

Piezoelectric beams provide a fast, high-force and scalable actuation mechanism that could offer precise motion control to medical microdevices including invasive micromanipulators, catheters and diagnosis tools. Their small displacement range can be addressed by motion amplification mechanisms. In this paper, a piezoelectric-actuated delta-robot actuator is proposed for probe-based confocal laser endomicroscopy (pCLE) microsystems. A prototype is designed and fabricated using three-dimensional (3D) polymer compound printing for a multi-flexure compliant motion amplifier and commercial piezoelectric beams. The flexure material is optimised for maximum linear output motion. The overall robot length is 76 mm and its maximum lateral dimension is 32 mm, with 10 g overall mass, including three piezoelectric beams. An axial motion control range of 0.70 mm and a maximum axial force of 20 mN are demonstrated, at 140 V actuation voltage. The proposed actuator architecture is promising for controlling lens, fibre and micromanipulator components for medical microrobotic applications.

Keywords: piezoelectric, compliant structure, motion amplification, flexure, stiffness gradient

(Some figures may appear in colour only in the online journal)

1. Introduction

A probe-based confocal laser endomicroscopy (pCLE), requires dynamic optical zoom and focus control in order to provide high-resolution confocal scanning in close proximity to the tissue surface. To expand the limited viewing range of pCLE systems [1], micro-motion fibre shifting has been proposed [2]. An actuation system with precise micro-motion

control for this application is highly desirable, in order to extend the range and the cell morphology characterisation capability of pCLE systems.

On the other hand, micro-motion actuation is very important to medical robotics in general. Such robots are not only used in optical control for medical microscopy [3, 4], but they are also extensively used in retinal microsurgery, intravascular surgery, robot-assisted biopsy, *in-vivo* assembly and advanced optics for surgery [5, 6]. A micro/nano-manipulation robot for medical applications often requires high accuracy, high dexterity, fast response speed and high repeatability to make sure operations are safe and efficient. Research and development for such systems often employ servo motors or tendon-driven catheters [7, 8]. The volume of such driving systems is relatively large and difficult to miniaturise.

* Author to whom any correspondence should be addressed.



Original content from this work may be used under the terms of the [Creative Commons Attribution 4.0 licence](https://creativecommons.org/licenses/by/4.0/). Any further distribution of this work must maintain attribution to the author(s) and the title of the work, journal citation and DOI.

In the last two decades, active-material-driven actuators have played a significant role in the miniaturisation of medical robots [9]. Those actuators can offer superior performance in power density, size and bandwidth terms. In addition, they provide flexibility of design and potential integration with electronics. They serve as the actuation mechanism of many micro medical devices [10, 11], surgical robots [12] and micro-robots [13], by utilising various transduction mechanisms, such as piezoelectric [14], thermo-responsive [11], electromagnetic [10] and electrostrictive [15] motion. Amongst these, piezoelectric actuators can provide faster response, more accurate motion and higher output force to weight ratio. Hence, high precision and high-frequency applications often employ piezoelectric transducers for actuation [10, 11, 16]. They usually have a large output force but a short working distance [17]. Conventional piezoelectric actuators include multilayer [18], tube [19], disk [20] and bender [21] types. In order to increase their working distance and achieve various motion types, piezoelectric benders can be combined with mechanical motion amplification systems [22]. Some of these systems employ flexure-based joints or distributed compliant structures. Structures of the latter type are designed for a distributed bending operation to avoid precision assembly steps and the wear or damage of joints during operation [12, 16, 23]. Systematic design approaches for compliant mechanisms have been proposed by Howell *et al* [24]. A review of compliant structures for piezoelectric actuators has been presented in [25].

In this paper, a piezoelectric-driven linear actuator is proposed for pCLE motion control. A flexure-based delta-robot architecture is employed, implemented by the combination of polymer compound three-dimensional (3D) printing and commercial piezoelectric beams. This is achieved by the use of a PolyJet 3D Printing equipment that allows the deposition of materials with controlled elasticity and even monolithic stiffness gradients on flexible joints [26]. The flexure structure and material design were optimised for maximum output displacement, using an experimental characterisation platform with synchronised electrical actuation and accurate output displacement monitoring presented in [25]. The flexure design and characterisation are presented in section 2. The fabrication method and the characterisation approach are discussed in section 3. The performance characterisation results and conclusions are presented in sections 4 and 5 respectively.

2. Flexure design

Flexure design is a key aspect of the functionality and performance of flexure-based compliant structures. On the one hand, flexures should be flexible enough to provide the desired displacement and force range at the actuation output. On the other hand, flexures should also have enough stiffness to sustain cyclic loading without plastic deformation. The behaviour of compliant flexures is difficult to simulate based on analytical models or finite element analysis because their mechanical properties depend on fabrication

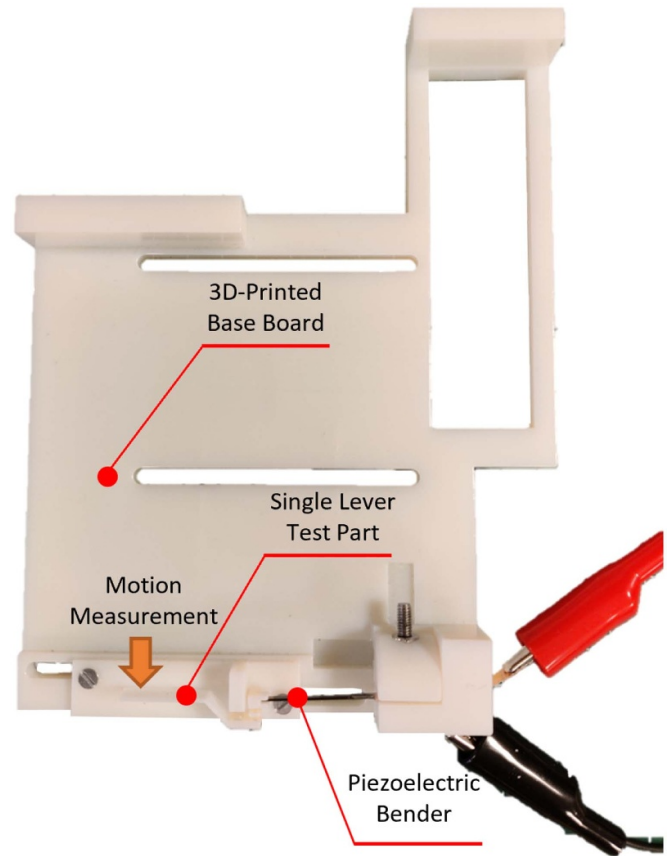


Figure 1. Photograph of the flexure evaluation setup.

details. Therefore, experimental characterisation of flexures is often preferable for designing a compliant structure.

Hence, an experimental study of performance for orthogonal block shape flexures composed of different polymer mixtures, using a Connex3 Objet500 Multi-Material 3D Printer was carried out. The advantage of employing multi-material 3D printing as a prototyping method includes the ability of compound composition based control of flexure elasticity as well as rapid prototyping and testing different designs. An also 3D-printed evaluation setup was used to allow synchronised piezoelectric actuation and precision motion monitoring. This setup is illustrated in figure 1. Devices with a range of material compositions and sizes were evaluated in terms of output displacement d_{out} and motion amplification $g = d_{out}/d_{in}$, where d_{in} is the input displacement provided by the active material device, which is a piezoelectric beam in this work. An indicative photograph of a lever with a 3 mm height flexure is presented in figure 2.

The measured scaling of d_{out} and g with material stiffness is shown in figure 3, indicating a maximum displacement of 0.6 mm at a rigid-to-soft polymer composition ratio at 70%, for this flexure geometry and the materials offered by the Connex3 Objet500 printer. While selecting this material composition can achieve maximum output displacement in the prototype device of this work, other flexure compositions can provide different output displacement/force balances, which may be

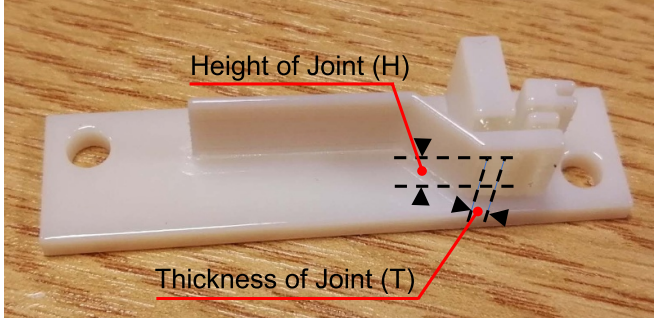


Figure 2. Photograph of a single lever indicating the flexure dimensions.

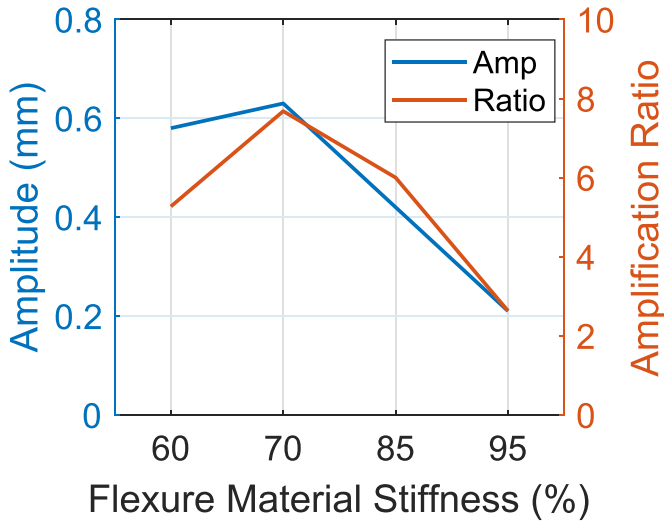


Figure 3. Measured amplified motion amplitude and amplification ratio of the single lever of figure 2, with a 3 mm high flexure [25].

preferable depending on the actuating apparatus properties and specifications. More details about this flexure design, fabrication and characterisation approach can be found in [25]. A characterisation of the rigid and soft polymers' performance in flexure structures can also be found in [25].

3. Fabrication and characterisation details

An axial motion actuator for manipulating endoscopy probes was designed and fabricated, with flexure designs selected with the characterisation method and results discussed in section 2. This actuator focuses on applying net axial displacement and force on a pCLE. Its design is based on a delta robot operation principle [16, 26] which is capable of three degrees of freedom (DOFs) motion. Its geometry maintains the top platform orientation on a fixed plane during motion regardless of any functional asymmetries of the actuating devices. In the experiments presented in this paper, the structure was tested for linear motion and actuating force. For this purpose, the delta-robot parallelogram mechanisms were removed from the design, fixing the actuation to axial motion. The three kinematics chains provide more actuation force and improve

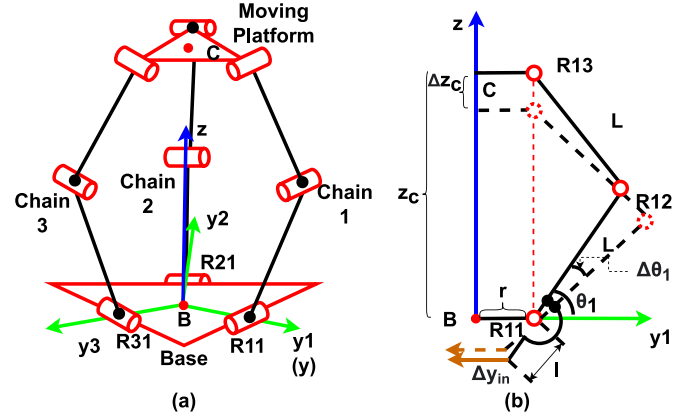


Figure 4. Schematic diagram of the geometry and kinematics of the compliant delta actuator: (a) overview. (b) Kinematical Chain 1.

motion linearity by symmetry-based cancellation of motion distortion.

The axial motion actuator consists of three kinematic chains, and each chain is actuated by a piezoelectric beam. The three kinematic chains are identical and rotationally symmetrical to each other with respect to the z -axis, as shown in figure 4(a). Each single chain comprises two arms of length L and three joints $Ri1$, $Ri2$ and $Ri3$, where $i = 1, 2$ and 3 , as detailed in figure 4(b). The displacement driven by the piezoelectric beam is applied at $Ri1$ and amplified, contributing to the z -axis motion of the moving platform. The closed-loop chains 1, 2 and 3 are coupled together to achieve platform motion only along the z -axis. This architecture is similar to the delta robot kinematics [27] but with fixed joints to restrict the C motion only along the z -axis. Point C is the geometry centre of the moving platform, at which the pCLE fibre may be attached. The design is illustrated in figure 5. The geometrical gain of a motion amplification mechanism can generally be defined as:

$$g = \frac{S_{out}}{S_{in}}, \quad (1)$$

where S_{out} and S_{in} are input and output displacements [22]. In figure 4, θ_i is the equilibrium value of each input angle of the compliant structure. Based on the static study presented in [25], for small-angle variations $\Delta\theta_i$, a linear relationship between the voltage applied to the piezoelectric beam and the radial displacement Δy_{in} can be assumed [28]:

$$|\Delta y_{in}| = \frac{3L^2}{2t} \cdot \frac{(1+B)(2B+1)}{AB^3 + 3B^2 + 3B + 1} \cdot d_{31} \cdot E_3 \quad (2)$$

where $A = \frac{E_m}{E_p}$, $B = \frac{t_m}{t_p}$, $t_m + 2t_p = t$. L is the total length of the piezoelectric bender, and t_m , t_p and t are the passive layer, piezoceramic layer and total beam thickness, respectively. d_{31} is the piezoelectric coefficient that relates the electric charge across ceramic plate thickness with an applied mechanical force along the bender's axial central line. $E_3 = \frac{V}{t_p}$ is the electrical field caused by the applied voltage V along t_p [29].

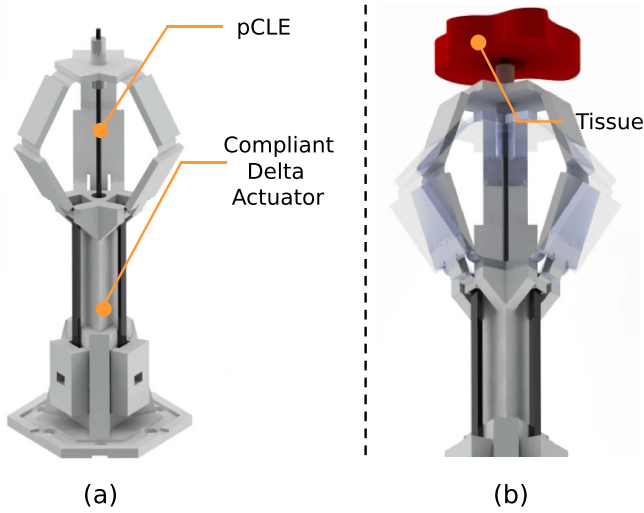


Figure 5. (a) Photorealistic schematic of the compliant delta actuator with a probe-based confocal laser endoscope (pCLE) fibre probe. (b) The working principle of the delta actuator. The actuator drives the pCLE to press human tissue for imaging, and it can also adjust the image quality through the vertical position of the probe.

The three kinematic chains are identical. The axial displacement of the moving platform can then be written as:

$$|\Delta z_c| = g \cdot \frac{(3L^2)}{2t} \cdot \frac{(1+B)(2B+1)}{AB^3 + 3B^2 + 3B + 1} \cdot d_{31} \cdot \frac{V}{t_p}, \quad (3)$$

where g is the geometrical gain provided by the kinematic chain arms, which after geometrical analysis can be written as:

$$g = \frac{|\Delta z_c|}{|\Delta y_{in}|} = \frac{2L}{l \cdot \tan \theta_i} \left(0 < \theta_i < \frac{\pi}{2} \right) \quad (4)$$

Equation (4) demonstrates that the axial motion gain scales with the kinematic chain length, L and with the inverse of the distance between the piezoelectric interface point and the rotation point of joint R11, l . It also scales with the cosine of the structure angle θ_i .

Two prototypes were fabricated and evaluated. In the first, the flexures were implemented geometrically, i.e. using the same rigid plastic material of the robot body, thinned down to allow bending in the desired direction. In the second, the flexures were implemented using a flexible, rubber-like composite material with suitable composition. In this paper, these joint implementations are referred to as plastic and rubber joints respectively. They are both considered to be compliant joints in the characterisation and analysis. Plastic joints are made in VeroWhite™, which is the same material used in the rigid device part. Rubber joints are made in the rubber-like digital material FLX9970 of the Connex3 Objet500 printer, which corresponds to the 70% composition identified in figure 3 for maximum displacement. The Computer Assisted Design (CAD) models of the two delta actuators are presented in figures 6(a) and (b).

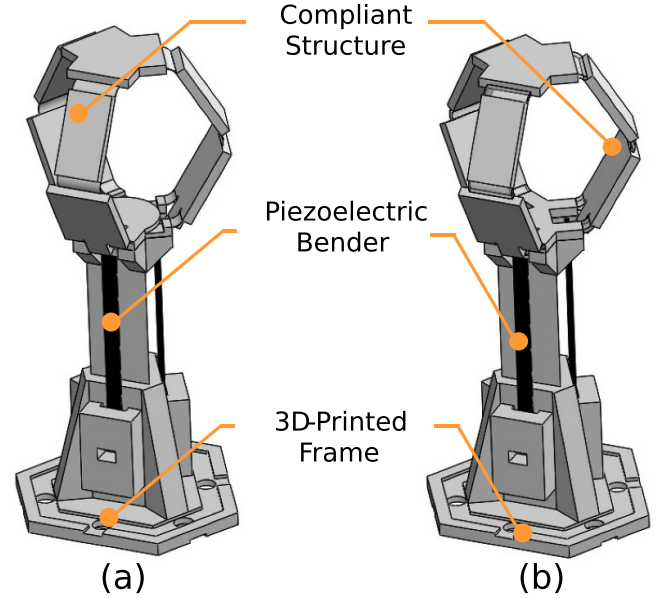


Figure 6. CAD models of the delta-robot actuator with (a) plastic and (b) rubber joint designs.

The plastic and rubber joints have an orthogonal block shape with 0.1 mm and 0.6 mm thickness respectively. This thickness difference was chosen such that both prototypes provide the same actuation displacement at 100 V actuation voltage. The fabrication procedure is presented in figure 7 using the rigid joint device design model. A suitable planar structure is 3D printed (figure 7(a)) and subsequently folded (figure 7(b)) and glued to its base, which is also 3D printed. The base design includes mounting slots for fixing three piezoelectric beams from Johnson Matthey [29]. The beams used are the Type 6 bending elements of the supplier catalogue [29] and their specifications are summarised in table 1.

3.1. Displacement characterisation platform

The experimental evaluation platform for the piezoelectric beam actuated delta robot consists of an optical table, an electrical actuation signal supply comprising an Aim-TTi TG5011A function generator, a Falco Systems WMA-300 voltage amplifier, a Keyence LK-G5000 laser displacement meter, a three-axis linear stage, and a 3D-printed structure for mounting the laser sensor. The overall experimental orientation is presented in figure 8. The electrical driving signal is produced by the generator, amplified by a factor of 50 by the voltage amplifier, and delivered to the three piezoelectric beams which are connected in parallel. Electrical connections to the piezoelectric pads were made using copper tape. Driving signals are exited from the generator, then 50 times amplified by the amplifier, and charged to the electrodes of the piezoelectric bender via conductive copper tapes. As shown in figure 8, the linear

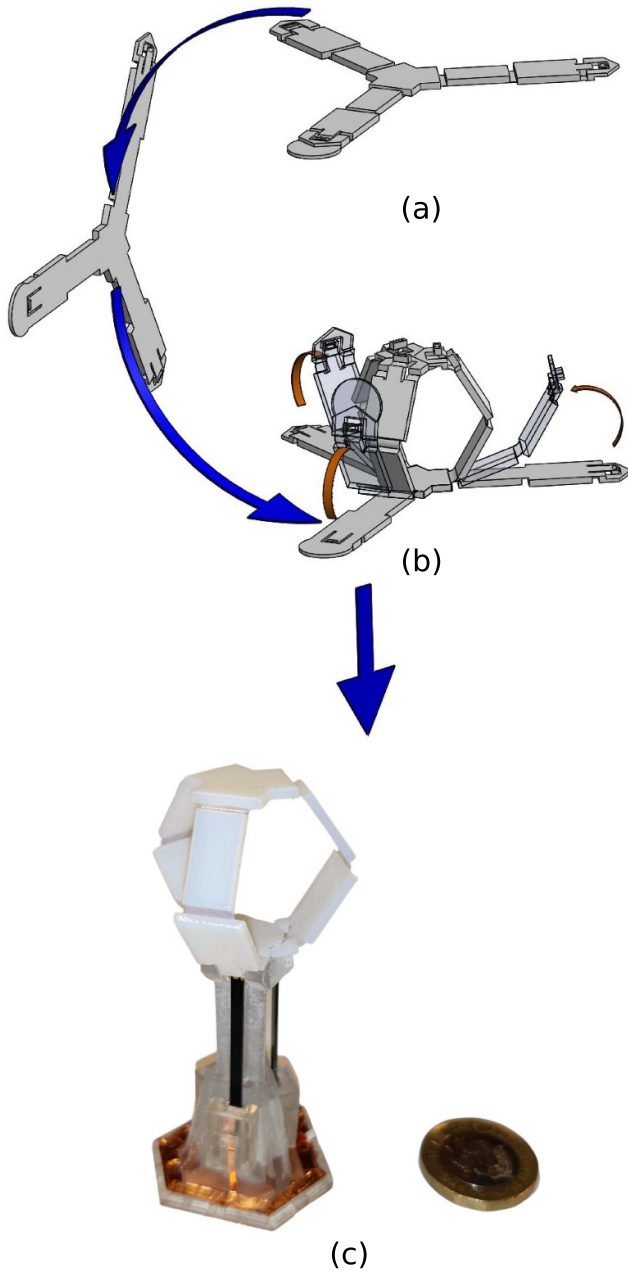


Figure 7. (a)–(b) Origami procedures to fabricate the actuators. (c) Realistic photo of the actuator with a one pound coin.

Table 1. Specifications of the JM Type-6 piezoelectric beam [29].

Parameters	Type 6	Parameters	Type 6
Total length (mm)	36.0	Total displacement (mm)	1.5
Free length (mm)	30.0	Blocking force (mN)	160
Width (mm)	2.1	Capacity per ceramic side (nF)	11
Thickness (mm)	0.67	Operating voltage (V)	230

delta actuator is placed under the laser sensor such that its vertical displacement can be accurately monitored during excitation.

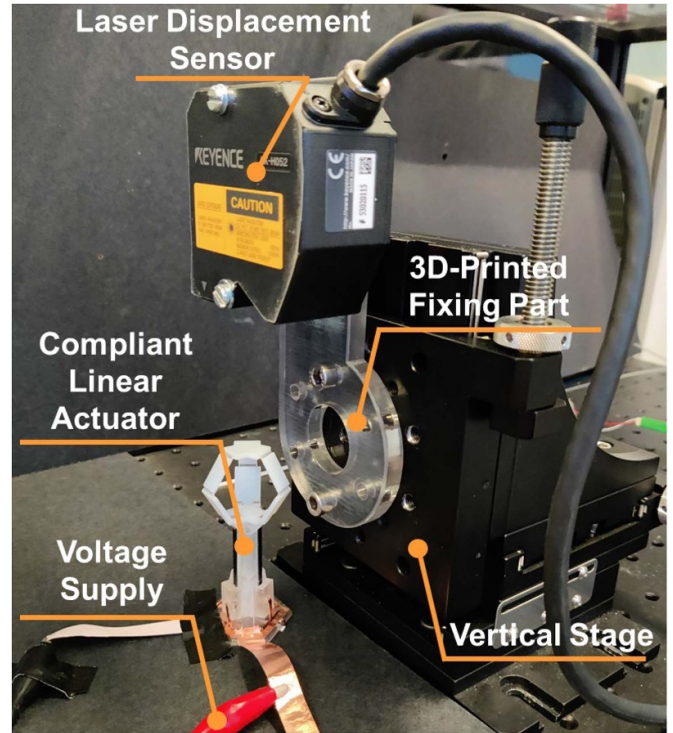


Figure 8. Experimental setup for the characterization of the compliant delta actuator prototypes.

3.2. Force characterisation method

The axial actuation force capability of the delta-robot prototypes was characterised in two experiments. In the first, the axial displacement caused by different mechanical loads was measured. For this purpose precision masses in the range of 0 g–10 grams were loaded on the top stage of the delta-robots. The final balance displacement was measured for various actuation voltages, ranging between 0 V and 140 V. This characterisation method is illustrated in figure 9. The actuator displacement due to each load was initially recorded without an actuation voltage (figure 9(a)). Subsequently, the displacement from the new (loaded) balancing position achieved by the application of different actuation voltages was measured (figure 9(b)). In this way, the actuator's mechanical response to different forces caused by tissue contact during pCLE measurements is emulated and characterised.

In the second experiment, the DC voltage value required to return the actuator to its unloaded balance position for each weight load is measured. Thereby, the force application capability of the actuator at zero displacements as a function of the applied voltage is characterised. This method is illustrated in figure 9(c). It involves placing a weight on the delta robot platform and recording the resulting displacement. Subsequently, the applied voltage is increased until the actuator recovers the displacement caused by gravity. Precision masses at 0.1 g steps were used for this purpose, until the actuators could not recover the displacement fully, even at maximum voltage. The results and discussion of these two experiments are presented in the following section.

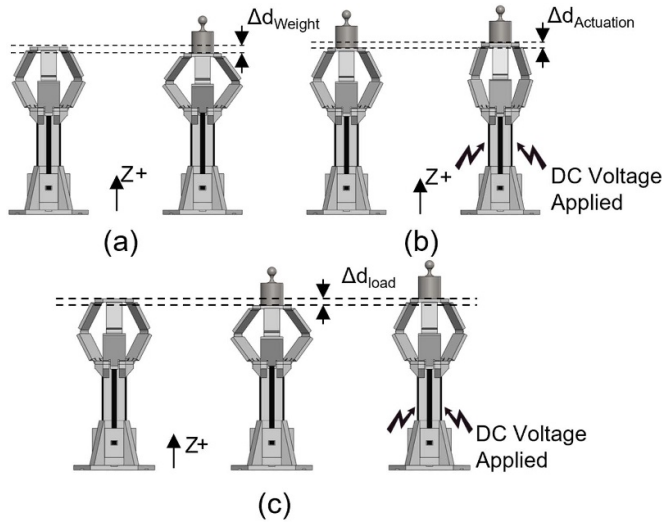


Figure 9. Schematic of the procedures to measure (a) the displacement caused only by weight. (b) The displacements driven by DC applied voltage. (c) The voltage maintaining the weights at initial positions.

4. Experimental results and discussion

4.1. Displacement characterisation

In figure 10(a), the measured displacement induced only by loading weights, without the application of an actuating voltage is presented as a function of load mass, for the plastic joint and the rubber joint prototypes. The displacement data correspond to average values from ten measurements at each voltage. The divergence of each measurement is included as error bars in the Figures.

A non-linear spring behaviour is observed in both cases. A parabolic fitting of the experimental data using an $F = az^2 + bz$ equation form, where F (mN) is the applied mass force, z (mm) is the absolute axial displacement and a (mN mm^{-2}), b (mN mm^{-1}) is stiffness parameters yields $(a_1, b_1) = (-21, 100)$ and $(a_2, b_2) = (-0.60, 19)$ respectively for the plastic and rubber joint prototypes. The displacements of the rubber joint actuator are generally more than three times bigger than those of the plastic joint actuator, and they reach 6.7 mm and 1.4 mm respectively at 10 g weight. Furthermore, the results reveal that the stiffness of the rubber actuator decreases with the moving platform closer to the base. The corresponding decrease for the plastic actuator is also apparent but significantly less than that of the rubber-joint prototype.

Furthermore, the capability of displacement actuation without load and under loads up to 10 g, was characterised by measuring the displacement as a function of applied voltage. Results for the plastic and rubber joint prototypes are shown in figures 10(b) and (c), respectively. Without load, a maximum displacement of 0.36 mm and 0.70 mm is obtained by the plastic and rubber joint prototype respectively. A linear fit of the measurements yields an actuation response of $2.5 \mu\text{m V}^{-1}$ and $5.1 \mu\text{m V}^{-1}$, respectively. The application of a mass load

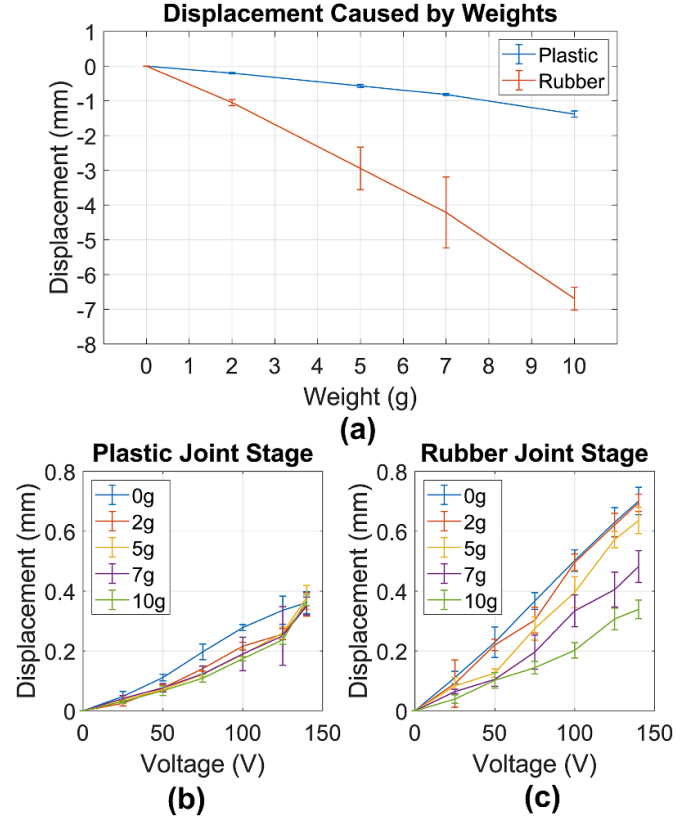


Figure 10. (a) Measured displacement caused by weight without actuation voltage. (b) and (c) Measured displacement as a function of applied voltage for the plastic (b) and the rubber (c) flexure actuator.

shifts the balancing position downward and generally reduces the actuation capability. Indicatively, the actuation responses at a 10 g load fall to $1.9 \mu\text{m V}^{-1}$ and $2.4 \mu\text{m V}^{-1}$ for plastic and rubber joints, respectively. This is as a reduction of approximately 24% and 53%, respectively.

Without a weight load, the maximum displacement of 0.36 mm and 0.70 mm was reached in 0.1 s and 1.5 s for the plastic and rubber joints respectively. This dynamic response corresponds to an average actuation speed of 3.2 mm s^{-1} and 0.44 mm s^{-1} respectively. The slower response of the rubber joint prototype is attributed to higher dynamic damping.

4.2. Force characterization

Figures 11(a) and (b) display the force characterisation results of the plastic and rubber joint delta actuator, respectively, following the method described in section 3.2. The blue curves show the displacement Δd_{load} caused by different precision mass loads. The weight range for the plastic and the rubber joint prototypes was 0 g–2 g and 0 g–1 g respectively. The orange curves show the corresponding DC voltage required to recover the occurred Δd_{load} for each mass. In this experiment the load mass range used is much smaller than the 0 g–10 g range of the results in figure 10, and the spring response observed is approximately linear. By linear fitting of the blue curves of figure 11, spring constants of 91 mN mm^{-1} and

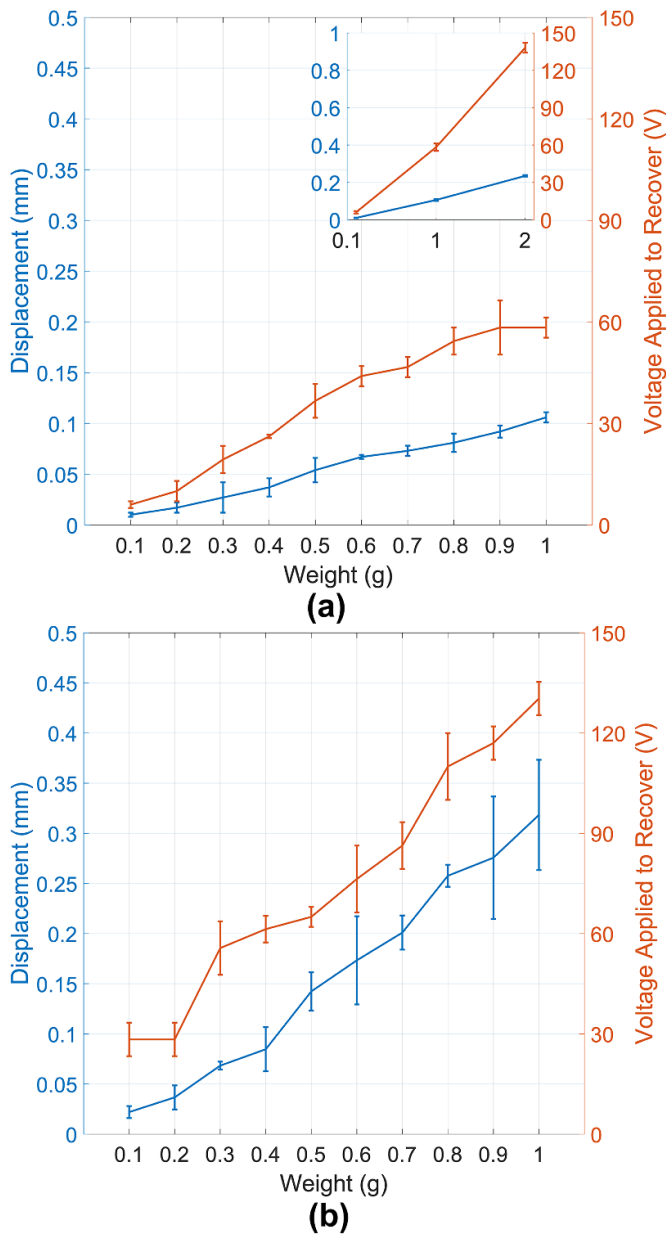


Figure 11. Measured displacement under a load mass and corresponding recovery voltage for the plastic (a) and rubber (b) joint prototypes. The full data of the plastic joint prototype is shown in the inset of (a), to maintain a common horizontal scale in the main diagrams for easy comparison.

29 mN mm⁻¹ are obtained for the plastic and rubber joint prototype respectively, for these loading ranges.

The recovery force follows a similar increasing trend. A measure of the force capability of the actuator as a function of applied voltage can be obtained by plotting the mass force data as a function of voltage as shown in figure 12. A maximum actuation force of 20 mN and 10 mN at zero displacements is demonstrated, by the application of 135 V for the plastic and the rubber joint prototype, respectively. By approximation of the increasing trends of figure 12 with linear fits, a force/voltage actuation performance parameter of 0.15 mN V⁻¹ (plastic joint) and 0.075 mN V⁻¹ (rubber joint) is obtained.

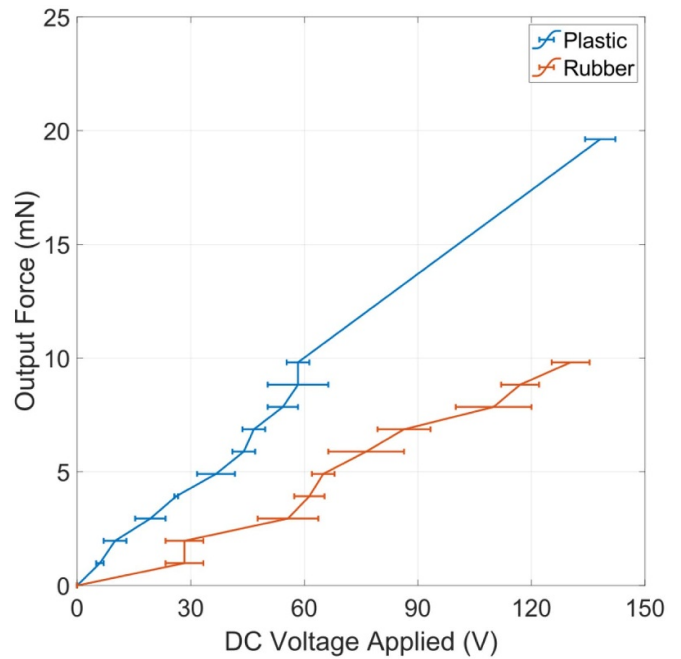


Figure 12. Actuation force at zero displacement calculated from the experimental results of figure 11.

5. Conclusion

In this paper, a modular experimental platform for the evaluation of piezoelectric-driven compliant structures is introduced. The characterisation experiments of the plastic and rubber joint delta actuators provide a complete performance indication for the actuation of optical components for endoscopy applications. Using precision mass weights as load emulators, a non-linear spring stiffness for both prototypes was observed. At the application of a 10 g mass, the plastic and rubber joint prototypes shifted their balance position by 1.40 mm and 6.70 mm respectively. A corresponding maximum displacement actuation of 0.36 mm and 0.70 mm was demonstrated within 0.1 s by the application of a 140 V bias voltage in parallel to the three piezoelectric benders. An overall actuation response was found of 2.5 $\mu\text{m V}^{-1}$ and 5.1 $\mu\text{m V}^{-1}$ respectively for the plastic and rubber joint prototypes. The application of a 10 g load reduced these values to 1.9 $\mu\text{m V}^{-1}$ and 2.4 $\mu\text{m V}^{-1}$, showing that significant actuation capability is maintained under constant loading. Finally, at zero displacements, a force/voltage actuation performance parameter of 0.15 mN V⁻¹ (plastic joint) and 0.075 mN V⁻¹ (rubber joint) was demonstrated. Depending on the application, a higher force or a higher displacement may be preferable, and in pCLE this also depends on the elastic properties of the optical fibre. The selectable flexure elasticity, using a 3D printed compound of suitable composition offers design adaptability to specific application implementations.

Further work may involve characterisation of the device's dynamic response, motion repeatability and closed-loop control based on position feedback. Position control may also address functional asymmetries among the actuating piezoelectric beams. An implementation of the proposed prototype

employing laser-cutting of titanium nickel alloy sheets may also be considered. The demonstrated results show promise for precision and scalable actuation from peripheral structures, which are of special interest for fibre medical robotics. The results presented here open up the way for demonstrating 3-DoF or even 6-DoF controlled motion, suitable for integration into a pCLE system for precise focus, zoom and angle control as well as other advanced optical functionalities including combinations with mechanical pressure actuation.

Data availability statement

All data that support the findings of this study are included within the article (and any supplementary files).

Acknowledgments

This work was financially supported by the Engineering and Physical Sciences Research Council (EPSRC), United Kingdom (EP/P012779, Micro-Robotics for Surgery). We would like to acknowledge Professor Andrew Holmes, Dr Khushi Vyas and Mr Jinshi Zhao for providing facilities.

ORCID iDs

Xu Chen  <https://orcid.org/0000-0002-2586-4556>

Michail E Kiziroglou  <https://orcid.org/0000-0002-0165-2508>

Eric M Yeatman  <https://orcid.org/0000-0003-0487-2693>

References

- [1] Capuano A *et al* 2019 The probe based confocal laser endomicroscopy (pCLE) in locally advanced gastric cancer: a powerful technique for real-time analysis of vasculature *Front. Oncol.* **9** 513
- [2] Vyas K, Hughes M, Rosa B G and Yang G-Z 2018 Fiber bundle shifting endomicroscopy for high-resolution imaging *Biomed. Opt. Express* **9** 4649–64
- [3] Aguirre A D, Sawinski J, Huang S-W, Zhou C, Denk W and Fujimoto J G 2010 High speed optical coherence microscopy with autofocus adjustment and a miniaturized endoscopic imaging probe *Opt. Express* **18** 4222–39
- [4] Chen X, Chen Z, Li X, Shan L, Sun W, Wang X, Xie T and Dong S 2016 A spiral motion piezoelectric micromotor for autofocus and auto zoom in a medical endoscope *Appl. Phys. Lett.* **108** 052902
- [5] Omisore O M, Han S, Xiong J, Li H, Li Z and Wang L 2022 A review on flexible robotic systems for minimally invasive surgery *IEEE Trans. Syst. Man Cybern.* **52** 631–44
- [6] Thomas T L, Kalpathy Venkiteswaran V, Ananthasuresh G K and Misra S 2021 Surgical applications of compliant mechanisms: a review *J. Mech. Robot.* **13**
- [7] Chi W *et al* 2020 Collaborative robot-assisted endovascular catheterisation with generative adversarial imitation learning *2020 IEEE Int. Conf. on Robotics and Automation (ICRA)* pp 2414–20
- [8] Wang J, Peine J and Dupont P E 2022 Eccentric tube robots as multiarmed steerable sheaths *IEEE Trans. Robot.* **38** 477–90
- [9] John S, Sirohi J, Wang G and Wereley N M 2007 Comparison of piezoelectric, magnetostrictive, and electrostrictive hybrid hydraulic actuators *J. Intell. Mater. Syst. Struct.* **18** 1035–48
- [10] Huang Y, Nakamura K, Takida Y, Minamide H, Hane K and Kanamori Y 2020 Actively tunable THz filter based on an electromagnetically induced transparency analog hybridised with a MEMS metamaterial *Sci. Rep.* **10** 20807
- [11] Ulkir O 2020 Design and fabrication of an electrothermal MEMS micro-actuator with 3D printing technology *Mater. Res. Express* **7** 075015
- [12] Suzuki H and Wood R J 2020 Origami-inspired miniature manipulator for teleoperated microsurgery *Nat. Mach. Intell.* **2** 437–46
- [13] Ghanbarzadeh-Dagheyan A, Jalili N and Ahmadian M T 2021 A holistic survey on mechatronic systems in micro/nano scale with challenges and applications *J. Micro-Bio Robot.* **17** 1–22
- [14] Liang C, Wang F, Huo Z, Shi B, Tian Y, Zhao X and Zhang D 2020 A 2-DOF monolithic compliant rotation platform driven by piezoelectric actuators *IEEE Trans. Ind. Electron.* **67** 6963–74
- [15] Li F, Jin L, Xu Z and Zhang S 2014 Electrostrictive effect in ferroelectrics: an alternative approach to improve piezoelectricity *Appl. Phys. Rev.* **1** 011103
- [16] McClintock H, Temel F Z, Doshi N, Koh J-S and Wood R J 2018 The milliDelta: a high-bandwidth, high-precision, millimeter-scale Delta robot *Sci. Robot.* **3**
- [17] Mohith S, Upadhyay A R, Navin K P, Kulkarni S M and Rao M 2020 Recent trends in piezoelectric actuators for precision motion and their applications: a review *Smart Mater. Struct.* **30** 013002
- [18] Zhou C, Duan J, Deng G and Li J 2017 A novel high-speed jet dispenser driven by double piezoelectric stacks *IEEE Trans. Ind. Electron.* **64** 412–9
- [19] Abdel-Gawad S and Wang X 2013 An improved model of thin cylindrical piezoelectric layers between isotropic elastic media *Int. J. Solids Struct.* **50** 4118–32
- [20] Haldkar R K, Khalatkar A, Gupta V K and Sheorey T 2021 New piezoelectric actuator design for enhance the micropump flow *Mater. Today* **44** 776–81
- [21] Chattaraj N and Ganguli R 2018 Performance improvement of a piezoelectric bimorph actuator by tailoring geometry *Mech. Adv. Mater. Struct.* **25** 829–35
- [22] Kiziroglou M E, Temelkuran B, Yeatman E M and Yang G-Z 2020 Micro motion amplification—a review *IEEE Access* **8** 64037–55
- [23] York P A, Peña R, Kent D and Wood R J 2021 Microrobotic laser steering for minimally invasive surgery *Sci. Robot.* **6** eabd5476
- [24] Howell L L, Magleby S P and Olsen B M (eds) 2013 *Handbook of Compliant Mechanisms* (Hoboken, NJ: Wiley)
- [25] Chen X, Kiziroglou M E and Yeatman E M 2021 Evaluation platform for MEMS-actuated 3D-printed compliant structures *2021 IEEE 20th Int. Conf. On Micro and Nanotechnology for Power Generation and Energy Conversion Applications (Powermems)* pp 188–91
- [26] Carrillo C S and Sanchez M 2021 Design and 3D printing of four multimaterial mechanical metamaterial using polyjet

- technology and digital materials for impact injury prevention 2021 43rd Annual Int. Conf. IEEE Engineering in Medicine Biology Society (EMBC) (November) pp 4916–9
- [27] Castillo Castaneda E, a G, García G and Bashir A 2006 Delta robot: inverse, direct, and intermediate Jacobians *Proc. Inst. Mech. Eng. C* **220** 103–9
- [28] Wang Q-M and Cross L E 1998 Performance analysis of piezoelectric cantilever bending actuators *Ferroelectrics* **215** 187–213
- [29] Johnson Matthey Piezo Products GmbH Bending actuators—johnson matthey piezo products (GmbH) (available at: www.piezoproducts.com/products-solutions/bending-actuators/)